Journal of Materials Chemistry B

ROYAL SOCIETY OF CHEMISTRY

PAPER

View Article Online
View Journal | View Issue

Cite this: J. Mater. Chem. B, 2025, 13, 10485

Mechanical strain-regulated hydrogel biodegradation for biological scaffolds with programmable lifetime

Akhiri Zannat,[a] Adolfo Lopez,[b] Yijie Cheng,[a] Jie Ma,[b] Mitchell Delemeester,[a] Shaoting Lin,[b] Krishnamurthy Jayaraman[a] and Xinyue Liu *[a]

Received 4th May 2025,
Accepted 30th July 2025

DOI: 10.1039/d5tb01056j

rsc.li/materials-b

Precise control over hydrogel biodegradation kinetics is of importance for drug delivery and tissue engineering. However, existing strategies usually rely on fixed material chemistries and offer limited tunability once implanted. Here, we introduce mechanical strain as a programmable cue to regulate hydrogel degradation *in situ*. Using peptide-crosslinked tetra-PEG hydrogels and proteinase K as a model system, we developed a real-time stress-monitoring platform to quantitatively study strain-dependent enzymatic degradation. Time-resolved measurements reveal that mechanical strain significantly accelerates degradation by simultaneously enhancing diffusion and reaction rates. For thick hydrogel samples, uniaxial stretching significantly reduces the degradation time by four-fold from 7.6 hours (undeformed) to 1.9 hours (stretched), shifting the process from slow, surface-limited to rapid, volumetric degradation. A multiscale theoretical model that we developed identifies three synergistic effects of mechanical strain: reduced diffusion path due to geometric thinning, increased network mesh size for enhanced enzyme penetration, and elevated chain tension that promotes bond cleavage. These findings establish mechanical loading as a universal tool in biological systems to dynamically modulate hydrogel lifetimes, offering new opportunities for programmable drug release and scaffold-guided tissue remodeling.

1. Introduction

Hydrogels are widely used as scaffold materials for hosting small-molecule drugs, biologics, and living cells in tissue regeneration and therapeutic applications.[1–4] Their high water content, tunable mechanical properties, biocompatibility, and biodegradability make them ideal candidates for implantation. Among these attributes, the biodegradation behavior of hydrogels plays a pivotal role in determining therapeutic efficacy and clinical outcomes.[5,6] Biodegradable hydrogels for implantation eliminate the need for secondary surgical removal and reduce the risk of chronic immune responses. More importantly, cotrolled degradation kinetics enables precisely timed therapeutic actions. For example, controlled drug release from a degradable matrix allows the release rate to be synchronized with systemic clearance or local biological demands.[7] Similarly, scaffold breakdown is designed to align with the dynamic stages of tissue repair, such as cellular infiltration, extracellular matrix deposition, and tissue remodeling, for enhanced integration and recovery.[8]

To achieve precise temporal control over hydrogel degradation, recent strategies have primarily focused on engineering the polymer chemistry to influence bond cleavage kinetics,

[a] Department of Chemical Engineering and Materials Science, Michigan State University, East Lansing, MI 48824, USA. E-mail: xyliu@msu.edu
[b] Department of Mechanical Engineering, Michigan State University, East Lansing, MI 48824, USA

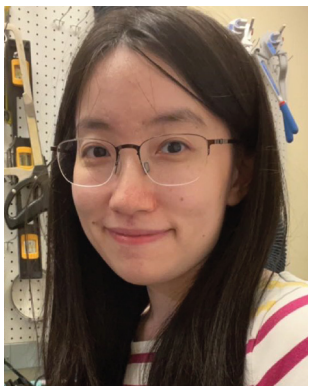

Xinyue Liu

Dr Xinyue Liu is an assistant professor in the Department of Chemical Engineering and Materials Science at Michigan State University. She received her PhD degree in Mechanical Engineering at Massachusetts Institute of Technology and BS degree in Polymer Material and Engineering from Sichuan University. Her research program focuses on designing hydrogel-based biomaterials at the interface of molecular chemistry, mechanics, optics, and living systems.

typically by incorporating cleavable crosslinkers (*e.g.*, ester,[9] disulfide,[10,11] or peptide bonds[12,13]) into the polymer backbone and modulating the local chemical environment.[14–18] In these systems, degradation behavior is predominantly dictated by fixed molecular architectures and relatively stable physiological conditions such as pH,[19,20] temperature,[21,22] and enzymatic composition.[23,24] As a result, the degradation profile is largely predetermined during fabrication and difficult to alter after implantation, limiting adaptability in dynamic biological environments. To introduce additional flexibility, external stimuli such as light[25–27] and ultrasound have been explored to activate specific bond-cleavage pathways.[28–30] These methods often function as binary triggers that switch degradation on or off, rather than enabling continuous modulation of degradation kinetics. This highlights a remaining gap in developing systems that allow for fine-tuned, externally regulated degradation kinetics.

In addition to intrinsic cleavage kinetics, the diffusion of water and catalytic species plays a critical role in the overall degradation process, particularly in bulky and non-porous polymer materials. In many cases, degradation is confined to surface regions, as enzymes or catalytic ions cannot efficiently penetrate the dense interior.[31–34] This reaction–diffusion coupling results in a significant delay in degradation, extending the complete timescale from hours (single-chain cleavage) to days or weeks (bulk material degradation). To address these transport limitations, several approaches have been developed such as incorporating hydrophilic segments,[13] creating loosely packed networks,[35] or introducing porosity[36] to enhance catalyst access. Nevertheless, these approaches are still predefined and do not allow on-demand or dynamic reprogramming of degradation profiles once the material is deployed.

Here, we introduce a fundamentally new design dimension that leverages mechanical strain as a dynamic regulator for hydrogel degradation. We hypothesize that the applied strain can simultaneously alter diffusion and reaction kinetics by altering the macroscopic geometry, microscopic network architecture, and single-chain extension of the hydrogel matrix. This multiscale control enables a shift in the degradation from a slow, surface-limited process to a rapid, volumetric degradation mode (Fig. 1a and b). To test this concept, we employ a model

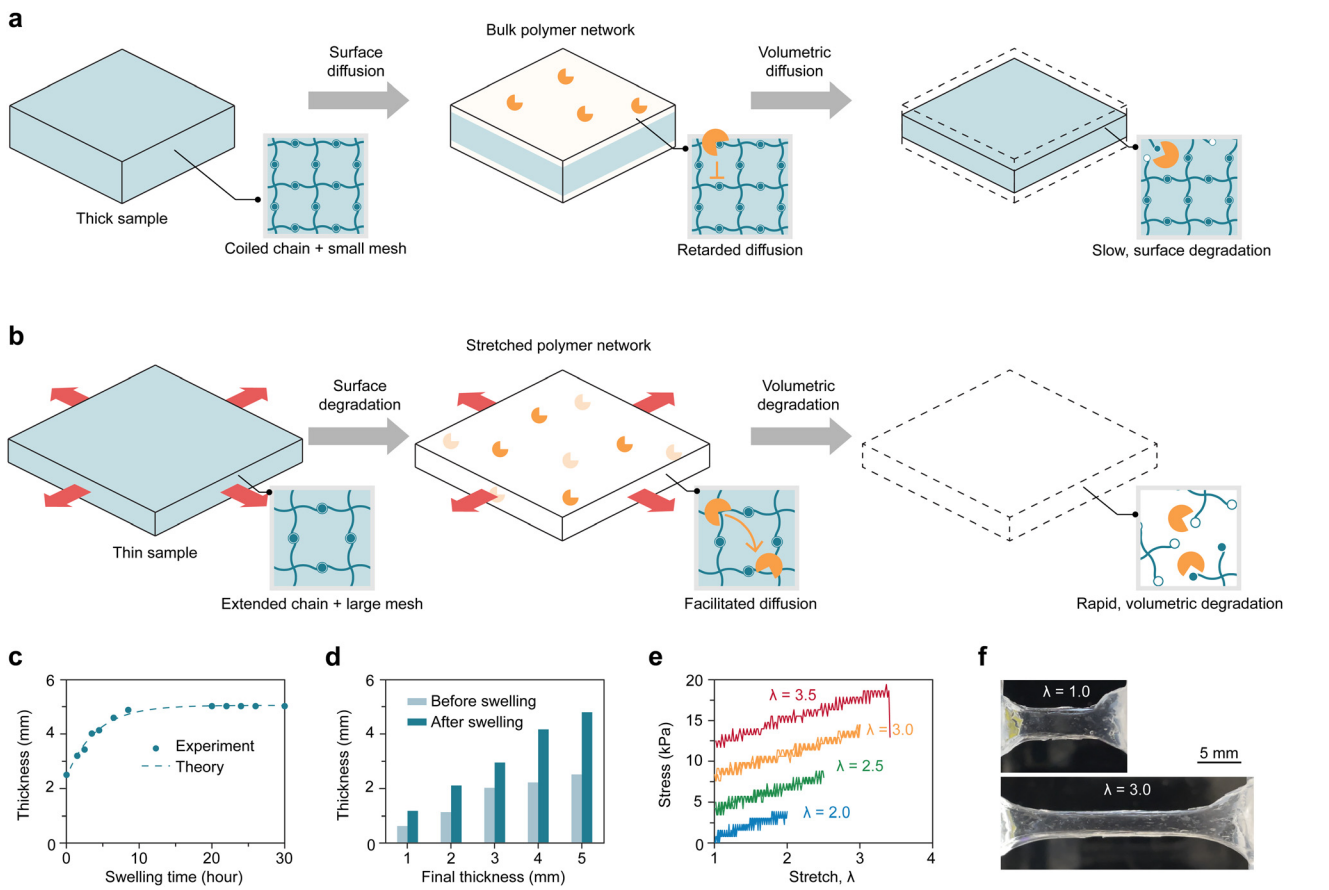

Fig. 1 Mechanical stretching affects enzyme-mediated hydrogel degradation. (a) In undeformed bulk hydrogels, the thick sample, small mesh size, and coiled polymer chains slow down enzyme diffusion and polymer degradation, leading to surface-limited degradation over prolonged timescales. (b) In mechanically deformed hydrogels, the thin sample, large mesh size, and extended-chain configuration facilitate enzyme penetration and enable rapid, volumetric degradation. (c) Time-dependent swelling behavior of an as-synthesized tetra-PEG hydrogel, whose thickness increases from 2.5 mm to 4.8 mm. (d) Tetra-PEG hydrogel thickness changes before and after swelling across five sample groups, showing a consistent swelling ratio of ~1.92. (e) Single-cycle stress–stretch curves for hydrogels stretched to different maximum ratios (λ = 2.0–3.5), showing high mechanical resilience and stretchability. (f) Images of hydrogel samples at rest (λ = 1.0) and under uniaxial stretch (λ = 2.5). Scale bar: 5 mm.

system of tetra-arm poly(ethylene glycol) (tetra-PEG) hydrogels end-crosslinked *via* peptide bonds, which are susceptible to enzymatic cleavage by proteinase K. Using a custom-built real-time characterization platform, we systematically quantify the time profiles of hydrogel degradation with varying characteristic dimensions and controlled uniaxial stretches. Our results reveal that applied mechanical strain strongly influences degradation time: in the absence of strain, a thick hydrogel exhibits diffusion-limited, surface-localized degradation, extending the complete degradation time to 3.5 hours. Remarkably, applying a high stretch ratio ($\lambda = 3.5$) restores the degradation time to 1.9 hours by enhancing enzyme penetration and bond scission throughout the entire volume. These experimental observations are well captured by a theoretical framework that couples reaction kinetics, enzyme diffusion, and mechanical deformation. The model identifies three synergistic roles of mechanical strain: (1) reducing diffusion path length by geometric thinning, (2) increasing network mesh size to enhance mass transport, and (3) elevating polymer chain tension to facilitate force-sensitive bond dissociation. Taking together, our findings established mechanical strain as a tunable approach to reprogram hydrogel degradation. This strain-responsive mechanism suggests new opportunities for designing next-generation biomaterials with on-demand, programmable lifetimes, particularly in applications such as tissue engineering scaffolds and drug delivery vehicles.

2. Results and discussion

2.1. Material and mechanics of the degradable tetra-PEG hydrogel system

Functional tetra-arm PEG macromers are known to form ideal polymer networks with minimal topological defects such as entanglements, loops, or dangling chains, resulting in hydrogels with highly uniform and tunable mechanical and transport properties.[37] We focused on the tetra-PEG hydrogel system to study enzyme-mediated degradation under mechanical strain, in which the well-defined and modular network architecture offers distinct advantages. First, the large and controllable mesh size (typically 5–40 nm) in tetra-PEG hydrogels[38] is comparable to or larger than the hydrodynamic radius of many enzymes (*e.g.*, 3–7 nm).[39] This allows catalytic species such as proteinase K to penetrate the hydrogel network efficiently, ensuring a high diffusivity of $\sim 10^{-10}$ m^2 s^{-1} and the diffusion timescale within experimentally accessible period (*i.e.*, several hours rather than days or weeks).[40] The short time frame enables the coupled reaction–diffusion processes can be systematically characterized. Second, tetra-PEG hydrogels are mechanically stretchable, with reported uniaxial fracture strain exceeding 200%, making them particularly suitable for investigating strain-dependent degradation behavior.[41] Third, the modular end-group chemistry of tetra-PEG macromers (*e.g.*, azide,[42] maleimide,[43] amine,[44] carboxyl,[45] acrylate,[46] thiol[47]) allows for a wide range of crosslinking strategies. In this study, we targeted amide bond (*i.e.*, peptide bond) crosslinking between tetra-amine-terminated PEG macromers (tetra-PEG-amine) and tetra-*N*-hydroxysuccinimide-terminated PEG macromers (tetra-PEG-NHS) to form a PEG network specifically degradable by proteinase K, a widely available broad-spectrum serine protease against peptide bonds. This enzymatic specificity provides a controllable platform for probing hydrogel degradation driven by crosslinking bond scission.

Tetra-PEG hydrogels were synthesized by mixing equimolar tetra-PEG-amine and tetra-PEG-NHS macromers (20 kDa, 5 kDa per arm) in buffer at a total PEG concentration of 100 mg mL^{-1}. This concentration is close to the overlap concentration, which is sufficient to facilitate efficient end-group crosslinking while minimizing inter- and intra-chain interactions.[48] Following crosslinking for over 12 hours, the precursor solution transitioned into a solid hydrogel, forming an ideal network with negligible defects. To generate samples with defined dimensions, the precursor solution was cast into dumbbell-shaped molds of varying thickness. The resulting hydrogels were then immersed in Tris-A buffer (0.05 M, pH 5.4) and allowed to swell to reach equilibrium for at least 30 hours (Fig. 1c and Fig. S1). All dimensions expanded uniformly with a swelling ratio of 1.92 in length (Fig. 1d), yielding final swollen thicknesses of 1.15 mm, 2.09 mm, 2.94 mm, 4.17 mm, and 4.80 mm, hereafter referred to as 1 mm, 2 mm, 3 mm, 4 mm, and 5 mm for simplicity.

To evaluate their mechanical response under tensile tension, we tested fully swollen, dumbbell-shaped hydrogel samples across a range of stretch ratios. Single-cycle stress–stretch curves showed negligible mechanical hysteresis from 2.0 to 3.5× stretch, indicating that the hydrogels exhibit excellent resilience and purely elastic behavior with minimal energy dissipation (Fig. 1e). The jagged appearance in the stress–stretch curves was attributed to instrumental noise arising from the limited sensitivity of the load cell. When held at a fixed stretch in Tris-A buffer, the hydrogels displayed no measurable stress relaxation over 17 hours (Fig. S2), confirming that they function as elastic solids under these conditions. The absence of delayed fracture or fatigue crack propagation during sustained tensile loading further supports the mechanical stability of the polymer network without catalytic species (Fig. S2). These results collectively demonstrate that any observed stress reduction during enzymatic degradation is not due to viscoelastic relaxation or fatigue failure, but rather to chemical degradation *via* crosslink cleavage. Thus, the time-dependent mechanical stress can serve as a direct and quantitative indicator of degradation kinetics. The hydrogels also exhibit a high stretchability, with a maximum elongation of $\sim$3.5 times their original length, allowing for testing across a wide range of strain conditions without mechanical failure (Fig. 1e and f). From the initial slope of the stress–stretch response, the Young's modulus was estimated to be approximately 3 kPa, consistent with the previously reported tetra-PEG hydrogel with a high reaction efficiency of 0.8.[49] Although some hydrolytic deactivation of NHS groups may lead to a small fraction of dangling chains, these imperfections do not significantly affect the overall mechanical performance or the reliability of degradation readouts.

We further characterized the viscoelasticity and morphology of synthesized tetra-PEG hydrogels prior to degradation using rheological measurements and scanning electron microscopy (SEM), respectively. Rheological analysis revealed that the storage modulus (G') remained constant and significantly higher than the loss modulus (G'') across the angular frequency range, suggesting rate-independent, solid-like response before degradation (Fig. S3a).[50] The as-synthesized hydrogels under SEM imaging confirm the intact and uniform surface morphology before degradation (Fig. S4a).

2.2. Real-time characterization of enzymatic degradation

To investigate hydrogel degradation under defined mechanical conditions, we developed a custom-built platform capable of real-time monitoring of tensile stress applied to hydrogel samples during enzymatic degradation. As shown in Fig. 2a and b, the platform integrates precise displacement adjustment, high-sensitivity force sensing, and a temperature-controlled, degradation solution-filled sample container. The hydrogel samples were uniaxially stretched using a screw-driven displacement system and held at a fixed strain. A miniature load cell with a capacity of 30 g and high sensitivity, paired with a signal conditioning amplifier, enabled accurate and continuous force readout at a sampling rate of 1 Hz over 4–8 hours. This configuration allowed us to detect small force changes associated with crosslink cleavage during degradation, which is typically in the range of 0–30 g (equivalent to 0–7.8 kPa, based on sample dimensions). Each dumbbell-shaped hydrogel sample was clamped between a fixed arm and the load cell, then fully submerged in the degradation medium consisting of 0.2 mg mL^{-1} proteinase K in Tris-A buffer (0.05 M, pH 8.0). The solution temperature was tightly regulated at 37.8 ± 0.4 °C, consistent with physiological conditions and within the optimal enzymatic activity range of proteinase K (Fig. 2c).[51–53] Despite slight water evaporation over the testing period, the degradation solution in the sealed sample container remained stable in both volume (46.7 ± 2.1 mL, Fig. 2d) and enzyme concentration (0.20–0.23 mg mL^{-1}), which ensures consistent degradation conditions.

To validate the mechanical readout as a reliable indicator of degradation kinetics, we prepared degradable and non-degradable tetra-PEG hydrogel samples and tested them in Tris-A buffer, with and without 0.2 mg mL^{-1} proteinase K. The degradable hydrogels, crosslinked *via* peptide bonds, maintained a stable stress level when stretched in buffer alone but exhibited a progressive decrease in tensile stress in the presence of proteinase K due to enzymatic cleavage of the crosslinks (Fig. 2g). This mechanical softening was visually confirmed by time-lapse imaging, where the hydrogel gradually lost structural integrity (t = 3 h) and ultimately disappeared (t = 6 h), indicating complete network disintegration (Fig. 2e). This degradation results in the formation of individual tetra-PEG macromers with amine and carboxyl terminal groups, which lack load-bearing capacity (Fig. 2f).[54] In contrast, non-degradable hydrogels were synthesized as a control by photopolymerizing tetra-acrylate-terminated PEG macromers *via* covalent carbon–carbon bond formation (Fig. 2h). Under a constant stretch of 2.0, the acrylate-crosslinked hydrogels maintained a constant tensile stress over time in both buffer and proteinase K solutions, confirming the chemical specificity of enzymatic degradation to peptide bonds and validating the robustness of the mechanical readout (Fig. 2i).

To further support the time-dependent degradation behavior, we characterized changes in the viscoelastic properties and surface morphology of tetra-PEG hydrogels (2-mm) under the same degradation conditions at different time points. Both the storage modulus (G') and loss modulus (G'') progressively decreased while the loss factor (G''/G') increased over the 4-hour degradation period (Fig. S3a–d). By the 4-hour time point, the storage and loss moduli both decreased to approximately 1 Pa, and the loss factor approached 1, suggesting a near-complete network breakdown into a highly compliant, viscoelastic state (Fig. S3c and d). The time-lapse SEM images demonstrated the increasingly heterogeneous surface and substantial mass loss over time due to the PEG enzymatic degradation (Fig. S4b and c).

To ensure safe application in biological contexts, we assessed the cytocompatibility of tetra-PEG hydrogels and their degradation products using live/dead cell viability assays. Culture media were pre-exposed to either intact hydrogels, partially degraded hydrogels, or fully degraded macromer products. Live/dead staining results demonstrated that all media conditions supported robust cell viability and proliferation with the viable cell fraction >90%. This indicates the biocompatibility of tetra-PEG hydrogels and their degradation products particularly for biomedical applications such as drug delivery and tissue engineering (Fig. S5).

2.3. Mechanical stretch mitigates the extended degradation time for large samples

In the absence of mechanical loading, degradation of bulky hydrogels proceeds slowly and is confined to the surface due to limited enzyme diffusion. We hypothesized that mechanical stretching could overcome this limitation by enhancing both enzyme transport and network susceptibility, with a transition to volumetric degradation even in millimeter-thick samples (Fig. 1a and b). To validate our hypothesis, we systematically quantified degradation kinetics across hydrogel samples with varying initial thicknesses (1–5 mm) and uniaxial stretch ratios (λ = 2.0 to 3.5), using the degradable tetra-PEG hydrogel system and real-time characterization platform (Fig. 3). The normalized stress–time profiles reveal that increased sample thickness slows down the degradation, indicated by prolonged stress retention (Fig. 3a–e). This delay is attributed to the longer diffusion paths for enzymes, which restrict enzymatic degradation primarily to surface layers in large hydrogels. Moreover, mechanical stretching significantly accelerates degradation, especially for the 4-mm and 5-mm samples (Fig. 3d and e). This enhancement likely arises from strain-induced reduction in effective diffusion resistance and increased polymer chain tension, both of which facilitate enzyme penetration and crosslink cleavage.

To quantitatively compare degradation behaviors, we defined a characteristic overall degradation timescale (τ_{tot}),

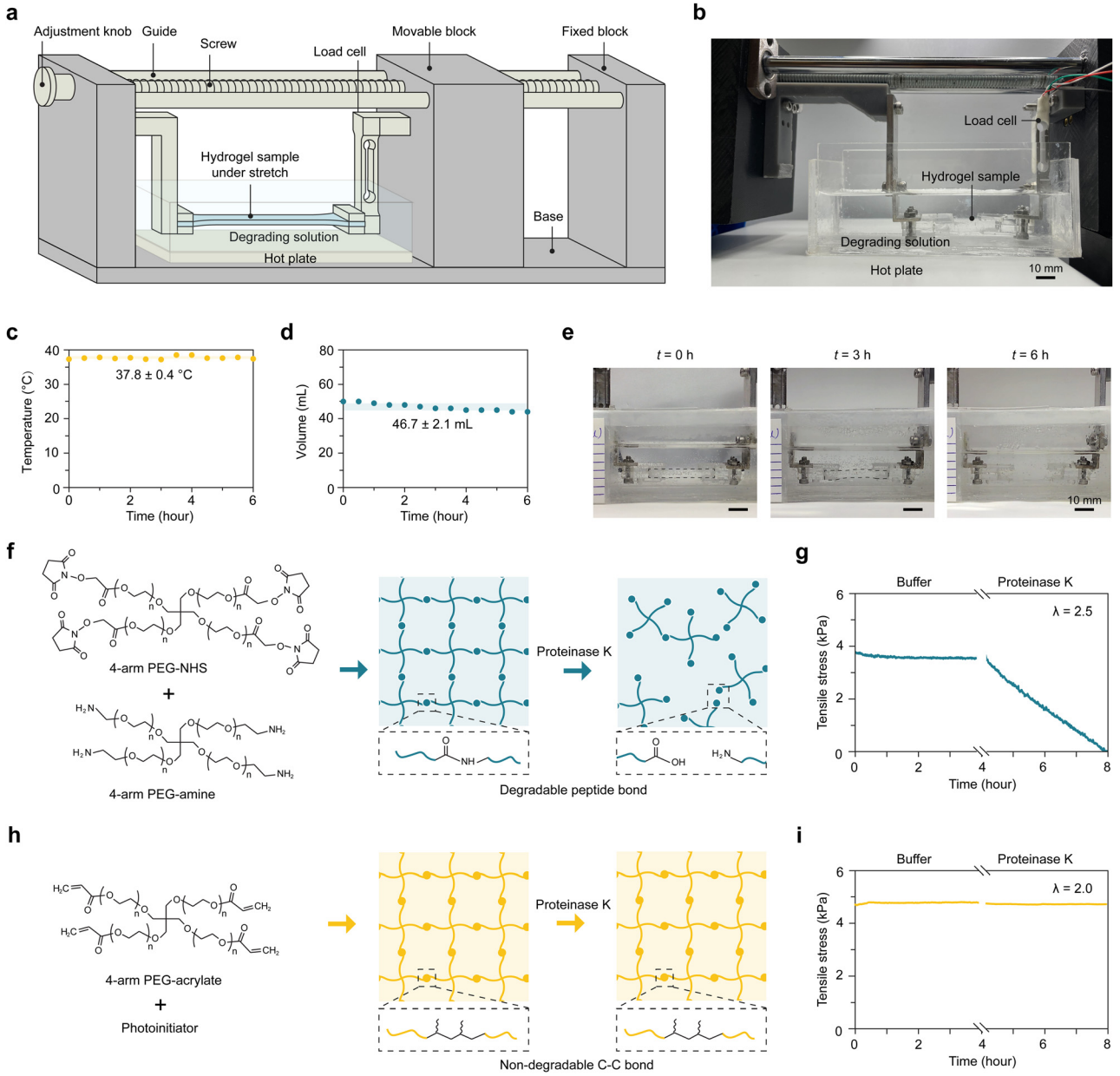

Fig. 2 Real-time mechanical stress monitoring platform for observation of hydrogel degradation under tensile strain. (a) Schematic of the custom-built platform for hydrogel degradation testing under constant tensile strain, featuring screw-driven displacement adjustment, a high-sensitivity load cell for real-time stress monitoring, and a temperature-controlled sample container maintained at 37 °C. (b) Image of the experimental setup showing a dumbbell-shaped tetra-PEG hydrogel sample clamped under uniaxial stretch and submerged in degrading solution (0.2 mg mL^{-1} proteinase K in Tris-A). Scale bar: 10 mm. (c) Temperature profile of the degradation solution, maintained at 37.8 ± 0.4 °C throughout the six-hour experiment. (d) Volume profile of the degradation solution, maintained at 46.7 ± 2.1 mL throughout the six-hour experiment, which confirms minimal evaporation. (e) Time-lapse images of the tetra-PEG hydrogel sample in the experimental setup at 0 h, 3 h, and 6 h, showing consistent sample positioning and solution level throughout the test. Dash lines depict the contours of the hydrogel sample in the degrading solution. Scale bars: 10 mm. (f) Chemical structure and degradation pathway of peptide-crosslinked tetra-PEG hydrogels, formed *via* amine–NHS chemistry and cleavable by proteinase K through peptide bond hydrolysis. (g) Stress–time curves of peptide-crosslinked tetra-PEG hydrogels under uniaxial stretch (λ = 2.0) in buffer and in degrading solution (0.2 mg mL^{-1} proteinase K in Tris-A). (h) Chemical structure and stability mechanism of acrylate-crosslinked tetra-PEG hydrogels, in which photopolymerized carbon–carbon crosslinks are resistant to enzymatic cleavage. (i) Stress–time curves of acrylate-crosslinked tetra-PEG hydrogels under uniaxial stretch (λ = 2.0) in buffer and in degrading solution (0.2 mg mL^{-1} proteinase K in Tris-A).

determined as the time at which the measured stress decayed to ~37% (*i.e.*, e^{-1}) of its initial value. These τ_{tot} values were extracted from each stress–time curve and compared with the theoretical predictions based on the additive contributions of the diffusion and reaction timescales ($\tau_{diff} + \tau_{deg}$, model details in Section 2.5). The results in Fig. 3f–j confirm that τ_{tot} consistently decreases with increasing stretch, with a more pronounced effect in thicker samples. The full dependence of

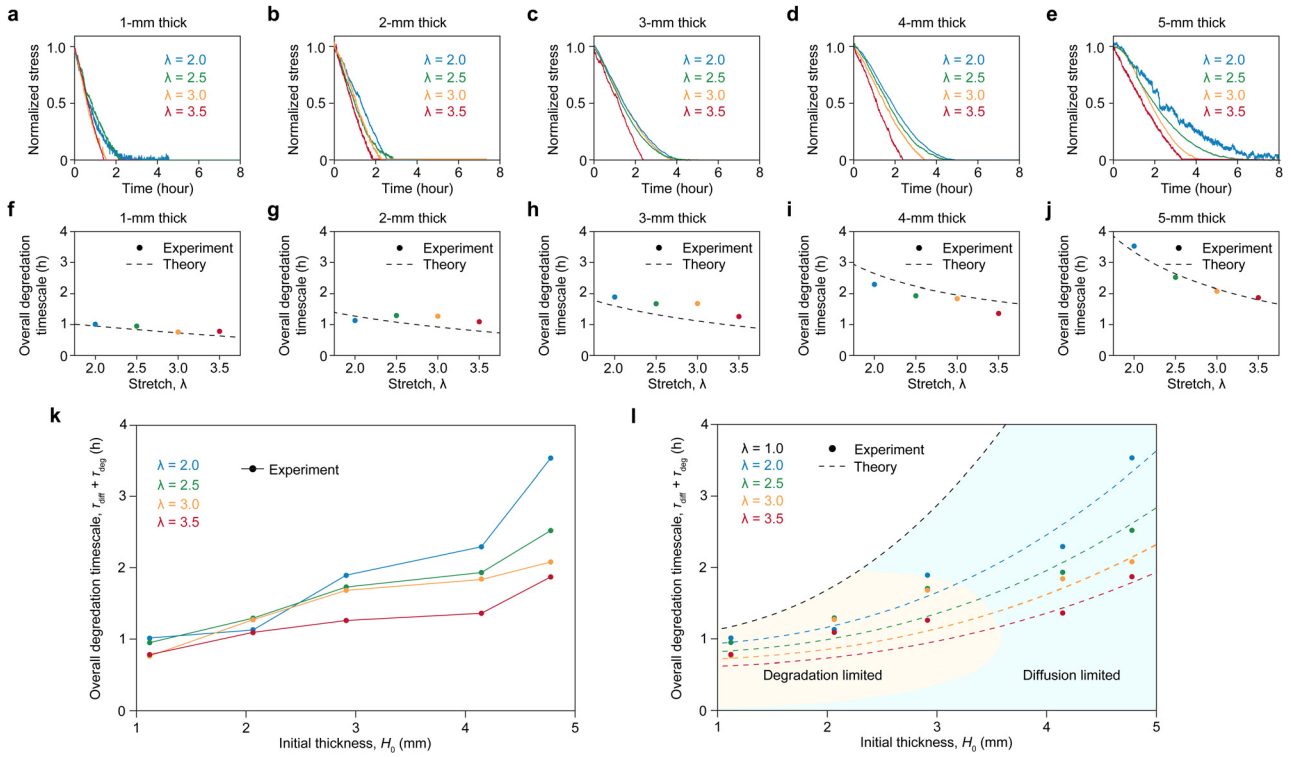

Fig. 3 Strain- and thickness-dependent hydrogel degradation kinetics characterized by real-time mechanical stress monitoring. (a)–(e) Normalized stress–time profiles for degradable tetra-PEG hydrogels with initial thicknesses of 1 mm (a), 2 mm (b), 3 mm (c), 4 mm (d), and 5 mm (e), each tested under different stretch ratios (λ = 2.0 to 3.5). (f)–(j) Corresponding overall degradation timescales ($\tau_{tot} = \tau_{diff} + \tau_{deg}$) as a function of stretch ratio (λ) for each hydrogel thickness. Solid dots represent experimental data, and dash lines represent theoretical predictions. (k) Experimentally measured overall degradation timescale ($\tau_{tot} = \tau_{diff} + \tau_{deg}$) as a function of initial hydrogel thickness (H_0) under different stretch ratios (λ = 2.0 to 3.5), showing a monotonic increase with thickness and modulation by applied strain. (l) Comparison of experimental (solid dots) and theoretical (dashed lines) overall degradation timescales ($\tau_{tot} = \tau_{diff} + \tau_{deg}$) as a function of initial hydrogel thickness (H_0) under different stretch ratios (λ = 1.0 to 3.5). The parameter space can be divided into degradation-limited ($\tau_{diff} < \tau_{deg}$) to diffusion-limited ($\tau_{diff} > \tau_{deg}$) regimes.

degradation timescales on thickness and stretch ratio is summarized in Fig. 3k and l. Although our setup does not allow direct measurement of stress changes during degradation of unstretched hydrogels (λ = 1.0), our theoretical calculation (Section 2.5) suggests that a 5-mm undeformed sample would require approximately 7.6 hours to degrade, compared to only 1.2 hours for a 1-mm sample (black dashed line, Fig. 3l). In contrast, when stretched to λ = 3.5, the degradation time of the 5-mm deformed sample is dramatically reduced to 1.9 hours. By comparing the diffusion timescale (τ_{diff}) and degradation timescale (τ_{deg}), we delineate two distinct regimes: a diffusion-limited regime ($\tau_{diff} > \tau_{deg}$, blue area in Fig. 3l) where transport constraints dominate in large samples under near-unstretched conditions; and a reaction-limited regime ($\tau_{diff} < \tau_{deg}$, yellow area in Fig. 3l) where bond cleavage is the rate-limiting step for small samples and highly stretched samples. These findings demonstrate that mechanical loading is an effective strategy to overcome diffusion barriers in large hydrogel structures, enabling more uniform and accelerated degradation.

2.4. Fluorescence recovery after photobleaching (FRAP) for enzyme diffusion analysis

To investigate how uniaxial strain affects molecular diffusion within hydrogels, we performed FRAP experiments on tetra-PEG hydrogels that are uniaxially stretched to defined ratios. FRAP uses a high-intensity laser to locally bleach fluorescent molecules and monitors the recovery of fluorescence intensity of the microscopic region over time, which reflects the in-plane diffusion of the fluorescent molecules in a matrix. We focused on two representative species: small-molecule fluorescein isothiocyanate (FITC, 0.3 kDa) and fluorescein isothiocyanate-labeled proteinase K (FITC-PK, 28.5 kDa). Hydrogels were incubated in either FITC (0.01 mg mL^{-1}) or FITC-PK (0.01 mg mL^{-1}) solutions for over 24 hours at 4 °C to achieve homogeneous fluorescent loading while minimizing enzymatic activity of proteinase K to prevent hydrogel degradation. No significant hydrogel softening or network disintegration was observed after the 24-hour incubation. FRAP experiments were conducted using a confocal laser scanning microscope (Olympus FluoView) with a 488-nm laser and a 20× objective lens. A central region on the hydrogel was bleached at 10 mW for 3 seconds, and fluorescence recovery was recorded over time.

Representative time-lapse images and fluorescence intensity recovery curves for FITC and FITC-PK are shown in Fig. 4a, b, e, and f, respectively. To extract the diffusion timescale, the recovery curves were fitted using the Soumpasis equation

$$\overline{I(t)} = e^{-\frac{\tau_{diff}}{t}}\left[B_0\left(\frac{\tau_{diff}}{t}\right) + B_1\left(\frac{\tau_{diff}}{t}\right)\right]$$

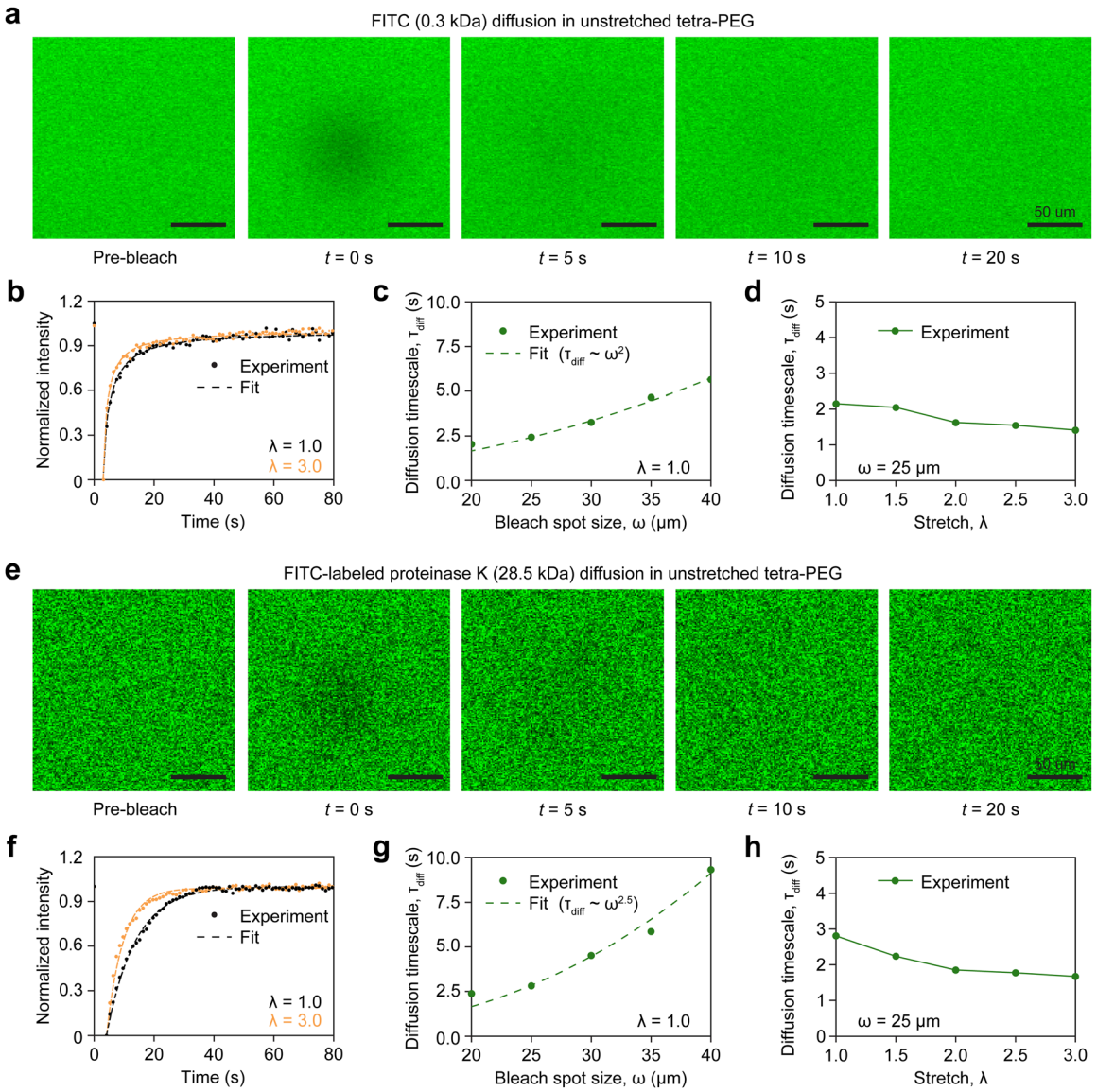

Fig. 4 Fluorescence recovery after photobleaching (FRAP) analysis of molecular diffusion in tetra-PEG hydrogels under tensile strain. (a) Representative time-lapse FRAP images showing the diffusion of FITC in an undeformed tetra-PEG hydrogel at pre-bleach, immediately post-bleach (t = 0 s), and during recovery (t = 5, 10, 20 s). Scale bars: 50 μm. (b) Representative fluorescence recovery curves of FITC at λ = 1.0 and 3.0. Dots represent experimental data, and lines represent fitting curves. (c) Diffusion timescales of FITC in tetra-PEG hydrogels as a function of bleach spot size without deformation (λ = 1.0). (d) Diffusion timescales of FITC in tetra-PEG hydrogels as a function of stretch ratios (λ = 1.0–3.0) at the constant bleach spot size of 25 μm. (e) Representative time-lapse FRAP images showing the diffusion of FITC-labeled proteinase K in an undeformed tetra-PEG hydrogel at pre-bleach, immediately post-bleach (t = 0 s), and during recovery (t = 5, 10, 20 s). Scale bars: 50 μm. (f) Representative fluorescence recovery curves of FITC-labeled proteinase K at λ = 1.0 and 3.0. Dots represent experimental data, and lines represent fitting curves. (g) Diffusion timescales of proteinase K in tetra-PEG hydrogels as a function of bleach spot size without deformation (λ = 1.0). (h) Diffusion timescales of proteinase K in tetra-PEG hydrogels as a function of stretch ratios (λ = 1.0–3.0) at the constant bleach spot size of 25 μm.

where $\overline{I(t)}$ is the normalized fluorescence intensity, t is the time, and B_0, B_1 are the modified Bessel function of the first kind (orders 0 and 1, respectively).[55] Fig. 4b and f plot the experimental data along with theoretical fitting curves, allowing us to extract the diffusion timescales (τ_{diff}). The complete dataset for all fluorescence intensity recovery curves is presented in Fig. S6. Compared to the small-molecule FITC, samples embedded with proteinase K exhibited a slower fluorescence recovery. For a 40-μm-diameter bleach spot, the diffusion timescale was significantly for FITC-PK (9.3 seconds) than for FITC (5.4 seconds) in the unstretched state, indicating greater hindrance to diffusion for the larger enzyme molecules. To further investigate the transport mechanism, we analyzed the dependence of τ_{diff} on bleach spot size (ω). For FITC, the diffusion timescale scaled as $\tau_{diff} \sim \omega^2$, consistent with classical Fickian diffusion (Fig. 4c). In contrast, FITC-PK followed a scaling of $\tau_{diff} \sim \omega^{2.5}$, deviating from Fickian behavior (Fig. 4g). This sub-diffusive behavior suggests that proteinase K with a

hydrodynamic diameter of ~6.7 nm experiences anomalous transport due to steric hindrance and obstruction from the tetra-PEG polymer network,[56] whose average mesh size of ~20 nm. Based on these results, we calculated the diffusion coefficients using

$$D = \frac{\omega^{\alpha}}{2\tau_{\mathrm{diff}}}$$

where α = 2 for Fickian diffusion of FITC and or α = 2.5 for obstructed diffusion of proteinase K. We further examined the effect of mechanical deformation by performing FRAP on hydrogels subjected to uniaxial stretch ratios ranging from 1.0 to 3.0. For both FITC and FITC-PK, we observed a mild decrease in the diffusion timescales (Fig. 4d and h) and a slight increase in diffusion coefficients with a higher stretch ratio (Fig. S7). These findings support our hypothesis that mechanical stretching can expand the mesh size and facilitate molecular transport, particularly for larger enzyme movement that is constrained by network architectures.

2.5. Theoretical modeling of coupled reaction–diffusion for strain effects

To elucidate the mechanism underlying strain-engineered degradation in the stretchable hydrogels, we develop a multi-scale, multi-physics theoretical model that quantitatively relates enzyme diffusion and polymer cleavage kinetics to macroscopic deformation. Our model integrates three distinct strain effects spanning from the macroscale (sample geometry) to microscale (polymer network structure) down to single-chain level (chain extension), all driven by the applied uniaxial stretch ratio λ (Fig. 5a–c).

2.5.1. Macroscopic geometry. When the hydrogel sample is stretched along one axis with a stretch ratio of λ_1 ($\lambda_1 = \lambda > 1$), the dimensions in the perpendicular directions decrease due to volume incompressibility ($\lambda_1\,\lambda_2\,\lambda_3 = 1$) (Fig. 5a, top). Assuming uniform transverse deformation ($\lambda_2 = \lambda_3$), the relationship between the stretched thickness (H) and the initial thickness (H_0) is derived as follows,

$$\lambda_2 = \lambda_3 = \frac{1}{\sqrt{\lambda}},\ H = \frac{H_0}{\sqrt{\lambda}}$$

Thus, at the macroscopic scale, uniaxial stretching reduces the sample's characteristic diffusion length (Fig. 5a, bottom), facilitating enzyme transport into the hydrogel interior.

2.5.2. Microscopic network. Each polymer strand in the tetra-PEG network has a molecular weight of approximately 10 kDa (two 5-kDa arms connected), corresponding to roughly 227 monomer units of ethylene glycol (–CH_2–CH_2–O–). Given that the Kuhn length (b) of PEG in water is 0.76 nm, equivalent to about two monomer unit length, each strand consists of N = 227/2 ≈ 114 Kuhn segments.[57] Therefore, the average end-to-end distance (R_0) of an individual strand in a good solvent (water) is estimated to be

$$R_0 = N^{3/5} b = 13\ \mathrm{nm}$$

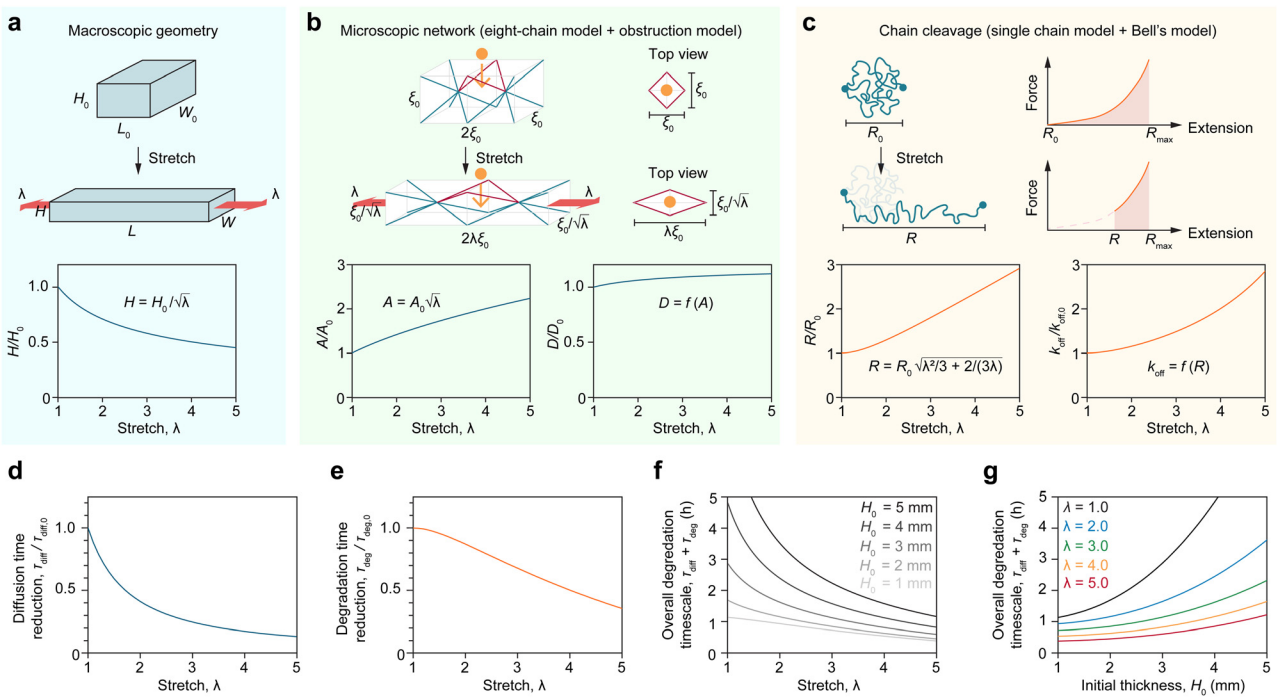

Fig. 5 Multiscale theoretical model describing strain effects on coupled reaction–diffusion kinetics in hydrogels. (a) At the macroscale, uniaxial stretching reduces the hydrogel thickness and shortens the diffusion length H. (b) At the microscale, stretching deforms the polymer mesh into a rhombus shape, increasing the projected mesh area A and enhancing the diffusion coefficient D. (c) At the chain level, polymer extension under stretch increases the end-to-end distance R and the force-dependent bond dissociation rate k_{off}. (d) Normalized diffusion time $\tau_{\mathrm{diff}}/\tau_{\mathrm{diff},0}$ decreases with an increasing stretch ratio. (e) Normalized degradation time $\tau_{\mathrm{deg}}/\tau_{\mathrm{deg},0}$ also decreases with an increasing stretch ratio. (f) Dependence of $\tau_{\mathrm{tot}} = \tau_{\mathrm{diff}} + \tau_{\mathrm{deg}}$ on stretch ratio under different initial thicknesses. (g) Dependence of $\tau_{\mathrm{tot}} = \tau_{\mathrm{diff}} + \tau_{\mathrm{deg}}$ on initial thickness under different stretch ratios.

which is also the mesh size ξ_0 in the tetra-PEG network and approximate to the side length in the eight-chain model.[50,59] Since the hydrodynamic diameter of the diffusing species (proteinase K, d = 6.7 nm) is smaller than the polymer mesh size, its diffusion within the hydrogel is modeled using an obstructed diffusion model, which treats polymer chains as randomly oriented rigid barriers that restrict species diffusion (Fig. 5b, top).[58]

To capture how uniaxial stretching affects polymer network geometry, we modeled the mesh unit in the eight-chain model[59] as a square with side length ξ_0 and area of A_0 at the unstretched state. Upon stretching, the unit deforms into a rhombus with side lengths $\xi_0/\sqrt{\lambda}$ (perpendicular to stretch) and $\xi_0\lambda$ (parallel to stretch). The projected mesh area available for enzyme diffusion is thus expanded by

$$\frac{A}{A_0} = \frac{\left(\xi_0/\sqrt{\lambda}\right) \times (\xi_0\lambda)}{{\xi_0}^2} = \sqrt{\lambda}$$

In the obstructed diffusion model, the diffusion coefficient D of a species with cross-sectional area $\pi d^2/4$, which can be described as a function of the mesh size A in the polymer network

$$D = D_{\text{liq}} \exp\left(-\frac{\pi d^2/4}{A}\right)$$

where D_{liq} is the diffusion coefficient of the chemical species in liquid without obstruction. Therefore, the diffusion coefficient under mechanical stretch (D), relative to the unstretched state (D_0), becomes

$$\frac{D}{D_0} = \exp\left[\frac{\pi d^2}{4}\left(\frac{1}{A_0} - \frac{1}{A}\right)\right]$$

Based on the dependence of mesh area on the stretch, the diffusion coefficient can be further simplified as

$$D = D_0 \exp\left[\frac{\pi d^2}{4{\xi_0}^2}\left(1 - \frac{1}{\sqrt{\lambda}}\right)\right]$$

These expressions quantitatively describe how mechanical deformation enhances molecular diffusion by expanding the polymer mesh dimensions (Fig. 5b, bottom).

2.5.3. Single-chain cleavage. When the hydrogel is deformed, individual polymer chains are stretched at the molecular level, increasing their end-to-end distance from R_0 to R. Compared to their relaxed coil state, extended chains require less additional energy to reach chain cleavage, leading to an increased bond dissociation rate (Fig. 5c, top). This mechanism can be described using a combination of the eight-chain model, the ideal chain Langevin model, and Bell's force-activated bond cleavage model.[60,61]

Based on the eight-chain model, we can correlate the single-chain extension to macroscopic deformation. The extended chain length R relative to the initial chain length R_0 is given by

$$\frac{R}{R_0} = \sqrt{\frac{{\lambda_1}^2 + {\lambda_2}^2 + {\lambda_3}^2}{3}}$$

Under uniaxial stretch of the hydrogel, $\lambda_1 = \lambda$ and $\lambda_2 = \lambda_3 = \frac{1}{\sqrt{\lambda}}$, the extended chain length can be simplified as

$$R = R_0\sqrt{\frac{\lambda^2}{3} + \frac{2}{3\lambda}}$$

Assuming chain length at the initial and maximally stretched states are $R_0 = N^{3/5}b$, and $R_{\max} = Nb$, where b is the Kuhn length and N is the number of Kuhn segments, we normalize the chain extension as

$$\frac{R}{Nb} = \frac{N^{3/5}b}{Nb}\sqrt{\frac{\lambda^2}{3} + \frac{2}{3\lambda}} = \sqrt{\frac{\lambda^2}{3N^{4/5}} + \frac{2}{3\lambda N^{4/5}}}$$

The ideal chain model[62,63] provides the relationship between chain extension and applied force on a single chain F by

$$\frac{R}{Nb} = \coth\left(\frac{Fb}{k_{\text{B}}T}\right) - \frac{k_{\text{B}}T}{Fb} = \mathcal{L}\left(\frac{Fb}{k_{\text{B}}T}\right)$$

where $\mathcal{L}$ is Langevin function, k_{B} is the Boltzmann constant and T is the temperature. Using the inverse Langevin function and substituting the expression for R/Nb, the force applied at the chain ends can be obtained as a function of hydrogel's stretch λ

$$\frac{Fb}{k_{\text{B}}T} = \mathcal{L}^{-1}\left(\frac{R}{Nb}\right) = \mathcal{L}^{-1}\left(\sqrt{\frac{\lambda^2}{3N^{4/5}} + \frac{2}{3\lambda N^{4/5}}}\right)$$

The bond dissociation rate k_{off} is also increased due to the applied force following Bell's exponential force-activation law

$$k_{\text{off}} = k_{\text{off},0}\exp\left(\frac{Fb}{k_{\text{B}}T}\right)$$

where $k_{\text{off},0}$ is the bond dissociation rate without any mechanical disturbance. Together, these relationships show that macroscopic uniaxial stretch increases chain extension and lowers the chain rupture energy barrier, which in turn accelerates bond cleavage (Fig. 5c, bottom).

2.5.4. Timescale analysis of diffusion and degradation. Based on the sub-diffusion scaling law validated in Section 2.4, the diffusion timescale under mechanical stretch is estimated as

$$\tau_{\text{diff}} = \frac{H^{2.5}}{D}$$

Substituting the abovementioned expressions for hydrogel thickness $H(\lambda)$ and diffusion coefficient $D(\lambda)$ under stretch, the relative diffusion timescale becomes

$$\frac{\tau_{\text{diff}}}{\tau_{\text{diff},0}} = \frac{1}{\lambda^{5/4}}\exp\left[-\frac{\pi d^2}{4{\xi_0}^2}\left(1 - \frac{1}{\sqrt{\lambda}}\right)\right]$$

where $\tau_{\text{diff},0}$ is the diffusion time without mechanical stretch. The base diffusivity D_0 was estimated from FRAP experiments performed on the undeformed samples. The corresponding diffusion time reduction as a function of stretch is shown in Fig. 5d.

On the other hand, the degradation reaction timescale is governed by the inverse of the force-dependent bond dissociation rate

$$\tau_{deg} = \frac{1}{k_{off}}$$

Based on Bell's model and the force–extension relationship derived from the inverse Langevin function, the relative degradation timescale under mechanical stretch is given by

$$\frac{\tau_{deg}}{\tau_{deg,0}} = \exp\left(-\frac{Fb}{k_B T}\right) = \exp\left[-\mathcal{L}^{-1}\left(\sqrt{\frac{\lambda^2}{3N^{4/5}} + \frac{2}{3\lambda N^{4/5}}}\right)\right]$$

where $\tau_{deg,0}$ is the degradation timescale without stretch. Based on literature values and our calibration, we set $\tau_{deg,0}$ = 1 hour. The degradation time reduction under stretch is shown in Fig. 5e.

Finally, we combined the strain-dependent diffusion and degradation behaviors to predict the overall degradation timescale: $\tau_{tot} = \tau_{diff} + \tau_{deg}$ as a function of initial thickness H_0 (Fig. 5f) and stretch ratio λ (Fig. 5g). Among the three strain-responsive mechanisms, macroscopic geometric changes dominate at low to moderate stretch ratios, primarily by reducing diffusion distance. At higher stretch levels, chain tension becomes increasingly significant by directly accelerating bond cleavage along strained polymer segments. This theoretical framework quantitatively recapitulates the experimentally observed strain-facilitated degradation and provides multiscale mechanistic insights that are not accessible through experimental characterization alone.

2.6. Mechanically regulated degradation enables controlled payload release

To demonstrate the functional impact of strain-modulated degradation for biomedical applications, we encapsulated

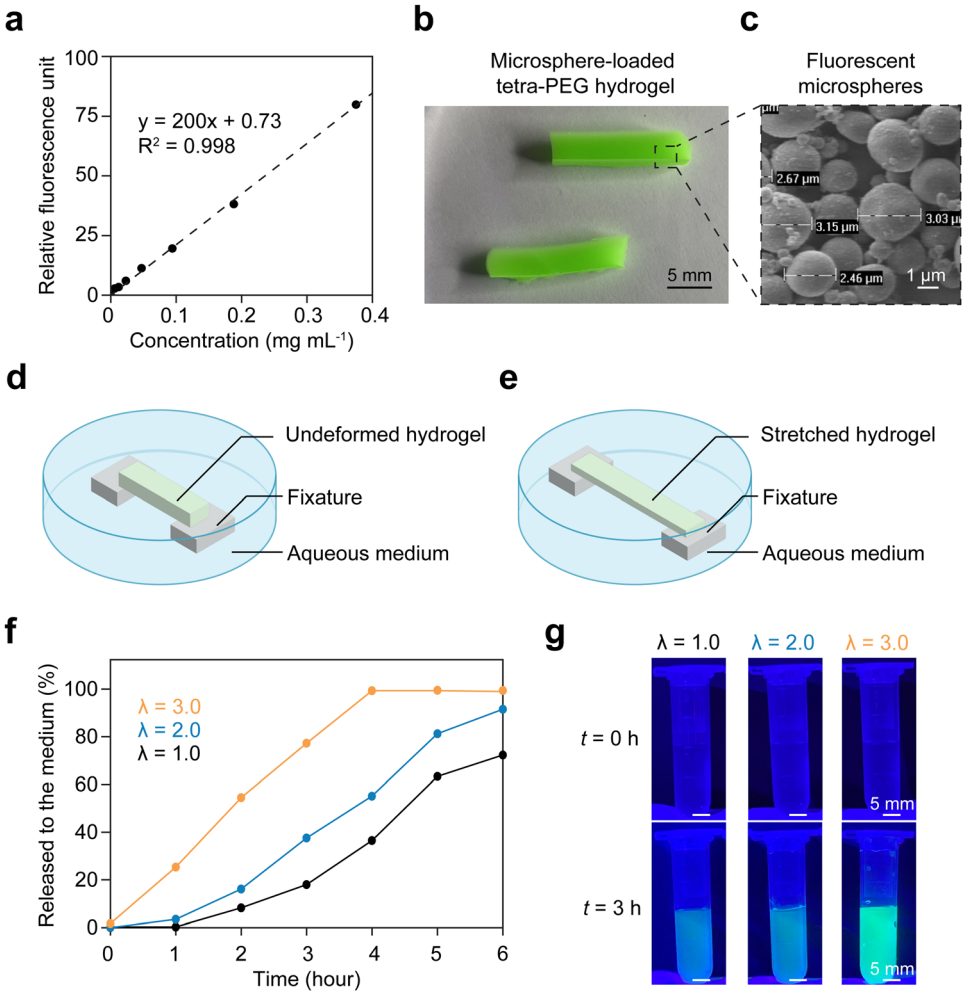

Fig. 6 Controlled release kinetics of encapsulated payloads modulated by mechanical stretch. (a) Calibration curve of relative fluorescence intensity *versus* concentration of fluorescent microspheres. (b) Image of tetra-PEG hydrogels that are loaded with fluorescent microspheres. Scale bar: 5 mm. (c) Scanning electron microscopy image of fluorescent microspheres with size annotated. Scale bar: 1 μm. Obtained from Cospheric LLC with permission. (d) and (e) Schematics of the experimental setup for the degradation and payload release of the undeformed (d) and stretched hydrogels (e) in the aqueous media. (f) Time-dependent release profiles of fluorescent microspheres from hydrogels under different uniaxial stretch ratios (λ = 1.0, 2.0, and 3.0). (g) Fluorescent images of the aqueous media collected before (t = 0 h) and during (t = 3 h) degradation and payload release. Scale bars: 5 mm.

fluorescent microspheres as model payloads within the degradable tetra-PEG hydrogels and evaluated their release profiles. Fluorescent microspheres were selected as model payloads for three key reasons: (1) fluorescence intensity provides a quantitative readout that correlates linearly with microsphere concentration in the surrounding medium (Fig. 6a); (2) their size range (1–5 μm) is comparable to that of particulate therapeutic carriers, such as synthetic microparticles, extracellular vesicles, viral vectors, or engineered microorganisms; (3) the dimension is orders of magnitude larger than the polymer mesh size (~13 nm), leading to negligible passive diffusion within the hydrogels and microsphere release occurring only when the polymer networks of hydrogels are enzymatically degraded (Fig. 6b and c).

The fluorescent microsphere-encapsulated hydrogels (4 mm in thickness after swelling) were uniaxially stretched to defined ratios and submerged in degradation medium (0.2 mg mL^{-1} proteinase K in Tris-A, pH 8.0) (Fig. 6d and e). The amount of released microspheres was monitored over time by tracking fluorescence levels in the medium. The release kinetics exhibited a strong dependence on applied mechanical strain (Fig. 6f and g). In undeformed samples (λ = 1.0), minimal release occurred within the first hour, and only ~35% of the encapsulated microspheres were released after four hours. Even after six hours, residual hydrogel remained, continuing to entrap fluorescent payloads. By contrast, hydrogels stretched to λ = 3.0 displayed rapid and complete release within four hours, with no solid hydrogel remnants observed. These release behaviors are consistent with the strain-dependent degradation kinetics measured previously (Fig. 3d), where complete degradation of stretched 4-mm-thick samples was achieved within the same timeframe. Together, the demonstration of mechanically programmable release of encapsulated payloads further validates the underlying degradation mechanism and highlights its translational potential for controlled drug delivery and tissue remodeling.

3. Conclusions

In this work, we established mechanical strain as a tunable and effective strategy for regulating hydrogel degradation kinetics. This concept was demonstrated using a stretchable, peptide-crosslinked tetra-PEG hydrogel and a custom-built real-time stress monitoring platform, which enable time-resolved analysis of enzyme-mediated degradation under mechanical load. Our results directly address the long-standing size-dependence challenge in polymer degradation, showing that applying uniaxial stretches can overcome diffusion bottlenecks and transform degradation from a slow, surface-only process to a rapid, volumetric response. Through a multiscale theoretical framework, we identified three key mechanisms by which strain accelerates degradation: geometric thinning that shortens diffusion paths, network mesh expansion that facilitates enzyme penetration, and polymer chain extension that promotes bond cleavage. These findings position mechanical loading as a versatile for tailoring hydrogel degradation and drug delivery profiles.

Looking forward, this mechanically responsive degradation strategy holds great potential for integration into dynamic biological systems, where mechanical cues are ubiquitous and continuous.[64] Strain can be applied through various pathways, including endogenous biological forces (*e.g.*, muscle contraction, joint movement, cardiovascular pulsation), remote mechanical stimulation techniques (*e.g.*, ultrasound, magnetic actuation), and pre-applied deformation during implantation. The material development combined with mechanical control opens new avenues for designing degradable biomaterials that adapt their degradation profiles in real time for a wide range of biomedical applications, including responsive drug delivery systems, wound healing matrices, tissue regenerative scaffolds, targeted cancer therapies, and temporary structural implants.[65]

4. Experimental section

4.1. Materials

The macromers for peptide-crosslinked tetra-PEG hydrogels, including tetra-PEG-amine (20 kDa), tetra-PEG-NHS (20 kDa), were purchased from Laysan Bio. For acrylate-crosslinked tetra-PEG hydrogels, the macromer, tetra-PEG-acrylate (20 kDa), was obtained from JenKem Technology, and the photoinitiator, 2-hydroxy-4′-(2-hydroxyethoxy)-2-methylpropiophenone (Irgacure 2959) was from Sigma-Aldrich. The degrading aqueous solution was maintained at pH 8.0 and included 0.2 mg mL^{-1} proteinase K (Gold Biotechnology), 0.05 M Tris A (Ambeed), and 0.04 M sodium hydroxide (Fisher Chemical). For FRAP experiments, FITC (0.3 kDa), FITC-PK (28.5 kDa), and phosphate buffered saline (PBS) were obtained from Sigma-Aldrich and Nanocs, respectively. In the payload release experiments, green fluorescent polymer microspheres (1.3 g mL^{-1}, particle size: 1–5 μm) were obtained from Cospheric.

4.2. Synthesis of peptide-crosslinked tetra-PEG hydrogels

Following a previously reported synthesis protocol,[66] we dissolved 100 mg of tetra-PEG-amine in 1 mL phosphate buffer (pH 7.4, ionic strength: 100 mM) and 100 mg of tetra-PEG-NHS in 1 mL phosphate-citric acid buffer solution (pH 5.8, ionic strength: 100 mM), respectively. The two solutions were mixed thoroughly and cast into a mold for crosslinking (>12 hours). The mold has a dumbbell shape with a gauge length of 5.5 mm, a width of 3.0 mm, and varied thicknesses from 0.6 mm, 1.1 mm, 1.5 mm, 2.2 mm, to 2.5 mm.

4.3. Synthesis of acrylate-crosslinked tetra-PEG-acrylate hydrogels

Tetra-PEG-acrylate hydrogels were prepared using tetra-PEG-acrylate macromers and the photoinitiator (Irgacure 2959). First, 1 mg of tetra-PEG-acrylate and 3 mg of Irgacure 2959 were dissolved in 1 mL deionized water and blocked from light by covering them with an aluminum foil. The solution was cast into a dumbbell-shaped mold with a gauge length of 5.5 mm, a

width of 3.0 mm, and a thickness of 1.5 mm, which was then exposed to UV light (365 nm; UVP CL-1000) for 1.5 hours.

4.4. Measurement of tetra-PEG hydrogel swelling

As-synthesized tetra-PEG hydrogels were immersed in Tris A solution and allowed to swell to equilibrium. The hydrogel dimensions (*i.e.*, thickness, width, gauge length) were measured at defined time points during the swelling using a digital caliper (Adoric). After 30 hours, equilibrium swelling was reached with a gauge length of 10.31 mm, a width of 5.76 mm, and the varied thicknesses from 1.15 mm, 2.09 mm, 2.94 mm, 4.17 mm, to 4.80 mm across different samples. The swelling ratio was defined as the ratio of the equilibrated (initial) and the as-synthesized (final) thickness. Swelling kinetics were obtained by plotting thickness over time and fitting to a mono-exponential rise model:

$$H_{\text{swell}}(t) = \left(H_{\text{swell}}(\infty) - H_{\text{syn}}\right)\left(1 - \mathrm{e}^{-\frac{t_{\text{swell}}}{\tau_{\text{swell}}}}\right) + H_{\text{syn}}$$

where t_{swell} is the swelling time, τ_{swell} is the characteristic time of swelling, H_{syn} is the as-synthesized hydrogel thickness before swelling, $H_{\text{swell}}(t)$ is the hydrogel thickness at time t, $H_{\text{swell}}(\infty)$ is the equilibrium hydrogel thickness.

4.5. Mechanical characterization of tetra-PEG hydrogels

We performed mechanical tests using a testing machine (CellScale UniVert) equipped with a 10 N load cell. Tetra-PEG hydrogel samples after synthesis and equilibrium swelling (gauge length: 10.45 mm, width: 5.47 mm, thickness: 4.17 mm) were mounted horizontally between two grips. Cyclic uniaxial tensile tests were first conducted by loading the samples to predefined stretch ratios (λ = 2.0, 2.5, 3.0, and 3.5), followed by unloading in each cycle. Then, we performed the stability tests with samples submerged in the Tris-A buffer (0.05 M, pH 5.4, no proteinase K) at 37 °C. The samples were stretched and held at a constant ratio of 2.5 for 17 hours, during which the tensile stress applied on the samples were recorded continuously.

4.6. Real-time stress-monitoring platform for hydrogel degradation characterization

To characterize the degradation kinetics of tetra-PEG hydrogels, a custom-built mechanical platform was developed, composed of (1) precise displacement control, (2) a temperature-controlled sample chamber filled with degradation solution, and (3) high-sensitivity force sensing (Fig. 2a). The displacement system consists of three interconnected blocks: two fixed blocks anchored to the base and one central movable block. These blocks are linked *via* a long screw and linear guides, enabling manual adjustment of the movable block to apply a defined uniaxial stretch to the hydrogel sample. Once the desired stretch is achieved, the system is locked in place to maintain constant strain during the degradation test.

During the degradation test, the hydrogel samples were clamped between two grippers and fully submerged in the degradation solution in a sample chamber. The degradation solution contains 0.2 mg mL^{-1} proteinase K in 0.05 M Tris-A buffer (pH 8.0). The solution temperature was maintained near 37 °C using a hot plate positioned beneath the chamber and monitored throughout the experiment using a digital thermometer. The chamber was sealed with a lid to reduce evaporation and protect the load cell from corrosion. To ensure consistent solution volume and concentration, a custom calibration scale was created by incrementally adding known volumes of buffer and marking the corresponding levels on the container. During testing, the solution level was visually checked every 30 minutes against this scale to monitor and maintain volume.

The tensile force is measured using a miniature high-sensitivity load cell (30 g capacity; strain measurement devices), which is mounted on the movable block and oriented vertically in a cantilever configuration. The hydrogel was gripped between the fixed and movable blocks, and as the hydrogel degraded, the real-time force transmitted through the hydrogel was detected by the load cell. Analog signals from the load cell were amplified using a SparkFun HX711 amplifier (gain: 128×) and digitized through an Arduino UNO Rev3 microcontroller board (sampling rate: 1 Hz). The digitized data were then transmitted *via* serial communication and recorded using CoolTerm software. Tensile stress was calculated using the equation:

$$\sigma = \frac{m \times 0.0098\ \text{N g}^{-1}}{W \times H}$$

where σ is the stress in pascals, m is the measured force in grams, and W and H are the sample width and thickness in meters, respectively.

4.7. Degradation tests for tetra-PEG hydrogels

Using the custom-built real-time stress-monitoring platform, we conducted degradation tests on both peptide-crosslinked and acrylate-crosslinked tetra-PEG hydrogels under controlled conditions. The peptide-crosslinked tetra-PEG hydrogel samples were first incubated in Tris-A buffer (0.05 M, pH 8.0) without proteinase K at 37 °C for four hours and then in enzyme-containing Tris-A buffer (0.05 M, pH 8.0) with 0.2 mg mL^{-1} proteinase K at 37 °C for an additional four-hour period. During the entire testing period, samples were uniaxially stretched and held at a constant stretch ratio of λ = 2.5, while tensile stress was continuously monitored. Acrylate-crosslinked hydrogel samples underwent the same incubation sequence, including 4 hours in buffer and 4 hours in enzyme solution, under identical temperature and buffer conditions. However, these samples were held at a lower stretch ratio of λ = 2.0, with stress monitored throughout the test. Furthermore, we systematically quantified degradation kinetics for peptide-crosslinked tetra-PEG hydrogel samples with varying initial thicknesses and uniaxial stretch ratios. The hydrogels with different thicknesses (1–5 mm) were subjected to enzyme-mediated degradation for 8 hours in Tris-A buffer (0.05 M, pH 8.0) containing 0.2 mg mL^{-1} proteinase K at 37 °C, under different constant stretch ratios (λ = 2.0 to 3.5). The recorded tensile stress was normalized to its initial value (at t = 0), and the overall degradation timescale (τ_{tot}) was defined as the time at which the normalized stress decayed to approximately 0.37.

4.8. Rheological measurements for tetra-PEG hydrogels

Rheological measurements were performed using a rotational rheometer (TA Instruments ARES 2) with a parallel plate fixture (diameter: 25 mm). Both plates were covered with adhesive-backed 220 grit sandpapers to eliminate the wall slip effect. The tetra-PEG hydrogels were synthesized, fully swollen, and exposed to identical degradation conditions (0.05 M Tris-A buffer, 0.2 mg mL^{-1} proteinase K, pH 8.0, 37 °C, λ = 1.0) for 0 hour, 2 hours, and 4 hours. After degradation, the tetra-PEG hydrogels were fitted into set gaps in the parallel plate fixture.

For the samples at 0 h, 2 h, and 4 h, the gap between the two plates was set at 2 mm, 1 mm, and 1 mm, respectively. First, the linear viscoelastic region of the material was identified with a shear strain sweep at an angular frequency of 1 rad s^{-1} on the 0 h degradation sample and a strain amplitude of 2% was selected for oscillatory frequency sweeps. The oscillatory angular frequency sweeps were conducted from 0.1 to 100 rad s^{-1} with a constant strain amplitude of 2% for the samples after 0 h, 2 h, and 4 h degradation. The storage modulus (G') and loss modulus (G'') were recorded to monitor the evolution of viscoelasticity of tetra-PEG hydrogels over the degradation process. The significant noise observed in G' and G'' for the 4-h sample is likely due to the torque resolution limits of the rheometer and sample heterogeneity (Fig. S3c).

4.9. SEM imaging for tetra-PEG hydrogels

SEM was used to investigate the surface morphology of tetra-PEG hydrogels after 0 h, 2 h, and 4 h degradation (0.05 M Tris-A buffer, 0.2 mg mL^{-1} proteinase K, pH 8.0, 37 °C, λ = 1.0). Samples were first lyophilized and then mounted onto aluminum SEM stubs using conductive carbon tapes. To enhance surface conductivity and prevent electron charging, the lyophilized samples were sputter-coated with a thin layer of gold. Using SEM (JEOL JSM-6610LV) under a high vacuum mode, we captured the surface morphology images at 200× and 3000× magnifications to analyze microstructural changes. Note that SEM imaging was performed on lyophilized samples due to the vacuum requirements of SEM. The lyophilization process removes water and can introduce artificial porosity that does not reflect the hydrogel's morphology under hydrated conditions.

4.10. Cytocompatibility test for tetra-PEG hydrogels

Cytocompatibility was evaluated using BT-549 human breast cancer cells (ATCC HTB-122, passage 7). Cells were cultured in complete Gibco RPMI 1640 medium (Life Technologies) supplemented with 10% fetal bovine serum (Sigma-Aldrich) and 1% penicillin–streptomycin (Life Technologies). To prepare test conditions, 3 mL of fresh culture medium was separately incubated for 12 hours at 37 °C with one of the following: (1) 0.25 g of tetra-PEG hydrogel after 0 h degradation, (2) 0.25 g of tetra-PEG hydrogel after 2 h degradation, (3) 0.5 g of tetra-PEG-amine macromer, or (4) 0.5 g of tetra-PEG-NHS macromer. The macromers represented fully degraded hydrogel products. After incubation, these media were termed pre-exposed media. BT-549 cells were detached using trypsin–EDTA, seeded into 96-well plates, and exposed to each pre-exposed medium for 48 hours at 37 °C. Cells cultured in fresh medium without treatment served as positive control, while cells treated with 70% ethanol for 1 minute served as negative control. All conditions were tested in triplicate (n = 3). Cell viability was quantified using the LIVE/DEAD viability/Cytotoxicity Kit (Life Technologies) following the manufacturer's protocol. The assay employed 4 μM calcein AM to stain live cells (green fluorescence) and ethidium homodimer-1 to stain dead cells (red fluorescence). Imaging was performed on a Leica TCS SP8 confocal microscope, with excitation/emission wavelengths of 495/515 nm for live cells and 495/635 nm for dead cells.

4.11. Fluorescence recovery after photobleaching (FRAP) test

Small-molecule fluorescein isothiocyanate (FITC, 0.3 kDa) and fluorescein isothiocyanate-labeled proteinase K (FITC-PK, 28.5 kDa) were used as the fluorescent probes in the FRAP experiments. Peptide-crosslinked tetra-PEG hydrogels (thickness: 0.6 mm) were incubated in FITC solution (0.01 mg mL^{-1} in PBS, pH 7.4) and FITC-PK solution (0.01 mg mL^{-1} in PBS, pH 7.4) for 15 hours, respectively. Incubation with FITC-PK was performed at 4 °C to minimize the enzymatic activity during labeling. After incubation, hydrogel samples were taken from the solution and gently cleaned with Kimwipes to remove residual surface liquid. Then, the samples were clamped to two grippers and uniaxially stretched to defined stretch ratios (λ = 1.0 to 3.0). FRAP experiments were performed using a spectral-based confocal laser scanning microscope (Olympus FluoView) with a 20× magnification objective and a 488 nm laser (10 mW). Circular regions with diameters of 20, 25, 30, 35, and 40 μm were selected to be subjected to photobleaching (100% laser power) for 0.3 seconds, respectively, resulting in a significant reduction of fluorescence within the regions. Subsequent fluorescence recovery in the regions was monitored over time by capturing time-lapse images at low laser intensity (0.5% laser power) to minimize additional photobleaching. Fluorescent intensity data was recorded and processed for further calculations.

4.12. Payload release kinetics measurement

A standard calibration curve was first established by preparing green fluorescent polymer microsphere suspensions in Tris A buffer at varying concentrations ranging from 0 to 0.375 mg mL^{-1}. Fluorescence intensity was measured using a Qubit 4 Fluorometer (Thermo Fisher Scientific) with the green fluorescence detection mode (excitation: 470 nm, emission: 515 nm). Microsphere-loaded, peptide-crosslinked tetra-PEG hydrogels were prepared following the similar protocol above while green fluorescent polymer microsphere were incorporated to the macromer precursor solution at a concentration of 88 mg mL^{-1}. The precursor solution was transferred to a rectangular mold (2.2 mm × 2.2 mm × 9.4 mm) to ensure a total microsphere payload of 4 mg per sample. The samples were swollen in Tris A buffer (4.2 mm × 4.2 mm × 18.0 mm), uniaxially stretched to defined ratios (λ = 1.0–3.0), and then incubated in 35 mL of degradation solution (0.2 mg mL^{-1} proteinase K in 0.05 M Tris-A

buffer, pH 8.0) at 37 °C. Fluorescence intensity of the degradation solution was measured every hour using the Qubit 4 Fluorometer to quantify microsphere release over time.

Author contributions

Akhiri Zannat and Xinyue Liu conceived and designed the study; Akhiri Zannat, Adolfo Lopez, Yijie Cheng, Jie Ma, and Mitchell Delemeester performed the experiments; Akhiri Zannat, Adolfo Lopez, Yijie Cheng, Jie Ma, Mitchell Delemeester, Shaoting Lin, Krishnamurthy Jayaraman, and Xinyue Liu analyzed the data; Akhiri Zannat and Xinyue Liu wrote the original draft and revised it with input from all authors.

Conflicts of interest

The authors declare no conflicting interests.

Data availability

The data supporting this article have been included as part of the SI. The original files will be made available upon request.

Additional kinetic characterization of tetra-PEG hydrogels. See DOI: **https://doi.org/10.1039/d5tb01056j**

Acknowledgements

We thank the members of the Center for Advanced Microscopy at Michigan State University, especially Melinda Frame, Abby Vanderberg, and Amy Albin, for their help in conducting FRAP and SEM experiments. This work was supported by the National Science Foundation (CBET2320716 and CBET-2401017), a Michigan State University faculty start-up grant, and the Tetrad Initiative.

References

1 J. S. T. Temeno and A. G. Mikos, *Biomaterials*, 2000, **21**, 2405–2412.
2 J. L. Drury and D. J. Mooney, *Biomaterials*, 2003, **24**, 4337–4351.
3 K. Y. Lee and D. J. Mooney, *Chem. Rev.*, 2001, **101**, 1870.
4 H. Tan and K. G. Marra, *Materials*, 2010, **3**, 1746–1767.
5 S. Rajeswari, T. Prasanthi, N. Sudha, R. P. Swain, S. Panda and V. Goka, *World J. Pharm. Pharm. Sci.*, 2017, **6**, 472–494.
6 M. Puertas-Bartolomé, A. Mora-Boza and L. García-Fernández, *Polymers*, 2021, **13**, 1209.
7 R. S. Petersen, L. H. Nielsen, T. Rindzevicius, A. Boisen and S. S. Keller, *Pharmaceutics*, 2020, **12**, 1050.
8 Y.-H. Kim, S. Vijayavenkataraman and G. Cidonio, *BMC Methods*, 2024, **1**, 2.
9 R. A. McBath and D. A. Shipp, *Polym. Chem.*, 2010, **1**, 860–865.
10 M. Braunreuther, J. Arenhoevel, R. Bej, C. Moose, M. A. Mall, R. Haag and G. G. Fuller, *Soft Matter*, 2025, **21**, 427–434.
11 I. G. Mercer, A. N. Italiano, I. G. Gazaryan, A. B. Steiner and S. V. Kazakov, *Gels*, 2023, **9**, 782.
12 A. Agrawal, E. M. Euliano, B. H. Pogostin, M. H. Yu, J. W. Swain, J. D. Hartgerink and K. J. McHugh, *Cell. Mol. Bioeng.*, 2024, **17**, 441–451.
13 C. M. Madl, L. M. Katz and S. C. Heilshorn, *ACS Macro Lett.*, 2018, **7**, 1302–1307.
14 R. Raman, T. Hua, G. Declan, J. Collins, T. Siddartha, Z. Jianlin, E. Tina, V. Soares, S. Pajovic, A. Hayward, R. Langer and G. Traverso, *Sci. Adv.*, 2020, **6**, eaay0065.
15 S. Bescós-Ramo, J. del Barrio, P. Romero, L. Florentino-Madiedo, M. Piñol and L. Oriol, *Macromolecules*, 2024, **57**, 10926–10937.
16 B. Hosseinzadeh and M. Ahmadi, *Mater. Today Sustainable*, 2023, **23**, 100468.
17 X. Zhang, L. Wang, H. Tao, Y. Sun, H. Yang and B. Lin, *Colloid Polym. Sci.*, 2019, **297**, 1233–1243.
18 F. M. Kelley, A. Ani, E. G. Pinlac, B. Linders, B. Favetta, M. Barai, Y. Ma, A. Singh, G. L. Dignon and Y. Gu, *Nat. Commun.*, 2025, **16**, 3521.
19 S. Li, *J. Biomed. Mater. Res.*, 1999, **48**, 342–353.
20 Y. Wang, G. A. Ameer, B. J. Sheppard and R. Langer, *Nat. Biotechnol.*, 2002, **20**, 602–606.
21 A. Göpferich, *The biomaterials: silver jubilee compendium*, 1996, pp. 117–128.
22 G. Pitt, M. Gratzl, G. Kimmel, J. Surles and A. Sohindler, *Biomaterials*, 1981, **2**, 215–220.
23 H. Tsuji and K. Suzuyoshi, *Polym. Degrad. Stab.*, 2002, **75**, 347–355.
24 Y. Tokiwa and B. P. Calabia, *Biotechnol. Lett.*, 2004, **26**, 1181–1189.
25 Y. Xing, B. Zeng and W. Yang, *Front. Bioeng. Biotechnol.*, 2022, **10**, 1075670.
26 X. Xu, Z. Zeng, Z. Huang, Y. Sun, Y. Huang, J. Chen, J. Ye, H. Yang, C. Yang and C. Zhao, *Carbohydr. Polym.*, 2020, **229**, 115394.
27 A. Göpferich and J. Teßmar, *Adv. Drug Delivery Rev.*, 2002, **54**, 911–931.
28 T. J. Yeingst, J. H. Arrizabalaga, F. S. Rawnaque, L. P. Stone, A. Yeware, A. M. Helton, A. Dhawan, J. C. Simon and D. J. Hayes, *ACS Appl. Mater. Interfaces*, 2023, **15**, 34607–34616.
29 M. K. DeBari, X. Niu, J. V. Scott, M. D. Griffin, S. R. Pereira, K. E. Cook, B. He and R. D. Abbott, *Adv. Healthcare Mater.*, 2021, **10**, 2100048.
30 S. Yamaguchi, K. Higashi, T. Azuma and A. Okamoto, *Biotechnol. J.*, 2019, **14**, 1800530.
31 S. M. Li, H. Garreau and M. Vert, *J. Mater. Sci.: Mater. Med.*, 1990, **1**, 123–130.
32 F. Von Burkersroda, L. Schedl and A. Göpferich, *Biomaterials*, 2002, **23**, 4221–4231.
33 G. Beamson, *The Scienta ESCA 300 Database*, 1992.
34 I. Grizzi, H. Garreau, S. Li and M. Vert, *Biomaterials*, 1995, **16**, 305–311.
35 M. M. H. Rumon, M. S. Rahman, A. A. Akib, M. S. Sohag, M. R. A. Rakib, M. A. R. Khan, F. Yesmin, M. S. Shakil and M. M. Rahman Khan, *Discovery Mater.*, 2025, **5**, 1–29.

36 Y.-C. Chiu, M.-H. Cheng, H. Engel, S.-W. Kao, J. C. Larson, S. Gupta and E. M. Brey, *Biomaterials*, 2011, **32**, 6045–6051.
37 G. A. Parada and X. Zhao, *Soft Matter*, 2018, **14**, 5186–5196.
38 D. Jia, Y. Tsuji, M. Shibayama and M. Muthukumar, *Macromolecules*, 2023, **56**, 9389–9397.
39 C. D. DiDomenico, M. Lintz and L. J. Bonassar, *Nat. Rev. Rheumatol.*, 2018, **14**, 393–403.
40 J. Liu and S. Lin, *J. Mech. Phys. Solids*, 2024, **191**, 105732.
41 T. Sakai, T. Matsunaga, Y. Yamamoto, C. Ito, R. Yoshida, S. Suzuki, N. Sasaki, M. Shibayama and U.-I. Chung, *Macromolecules*, 2008, **41**, 5379–5384.
42 R. T. Chen, S. Marchesan, R. A. Evans, K. E. Styan, G. K. Such, A. Postma, K. M. McLean, B. W. Muir and F. Caruso, *Biomacromolecules*, 2012, **13**, 889–895.
43 E. A. Phelps, M. N. O. Enemchukwu, M. V. F. Fiore, J. C. Sy, N. Murthy, T. A. Sulchek, T. H. Barker and A. J. García, *Adv. Mater.*, 2011, **24**, 64.
44 X. Liu, L. Zhang, B. El Fil, C. D. Díaz-Marín, Y. Zhong, X. Li, S. Lin and E. N. Wang, *Adv. Mater.*, 2023, **35**, 2211763.
45 K. A. Rose, E. Marino, C. S. O'Bryan, C. B. Murray, D. Lee and R. J. Composto, *Soft Matter*, 2022, **18**, 9045–9056.
46 Y. Hao, H. Shih, Z. Muňoz, A. Kemp and C.-C. Lin, *Acta Biomater.*, 2014, **10**, 104–114.
47 Z. Meng, L. Löser, K. Saalwächter, U. Gasser and H.-A. Klok, *Macromolecules*, 2024, **57**, 3058–3065.
48 T. Matsunaga, T. Sakai, Y. Akagi, U.-I. Chung and M. Shibayama, *Macromolecules*, 2009, **42**, 1344–1351.
49 D. Zheng, S. Lin, J. Ni and X. Zhao, *Extreme Mech. Lett.*, 2022, **51**, 101608.
50 M. Rubinstein and R. H. Colby, *Polymer physics*, Oxford University Press, 2003.
51 W. Bangning, H. Buxing and T. Fu, *J. Therm. Anal. Calorim.*, 1997, **50**, 73–80.
52 J. Dattagupta, T. Fujiwara, E. Grishin, K. Lindner, P. Manor, N. Pieniazek, W. Saenger and D. Suck, *J. Mol. Biol.*, 1975, **97**, 267–271.
53 W. Ebeling, N. Hennrich, M. Klockow, H. Metz, H. D. Orth and H. Lang, *Eur. J. Biochem.*, 1974, **47**, 91–97.
54 R. Reid, M. Sgobba, B. Raveh, G. Rastelli, A. Sali and D. V. Santi, *Macromolecules*, 2015, **48**, 7359–7369.
55 D. Soumpasis, *Biophys. J.*, 1983, **41**, 95–97.
56 C. R. Picu, *Soft Matter*, 2011, **7**, 6768–6785.
57 D. J. Waters, K. Engberg, R. Parke-Houben, L. Hartmann, C. N. Ta, M. F. Toney and C. W. Frank, *Macromolecules*, 2010, **43**, 6861–6870.
58 B. Amsden, *Macromolecules*, 1999, **32**, 874–879.
59 E. M. Arruda and M. C. Boyce, *J. Mech. Phys. Solids*, 1993, **41**, 389–412.
60 E. B. Walton, S. Lee and K. J. Van Vliet, *Biophys. J.*, 2008, **94**, 2621–2630.
61 K. Yu, A. Xin, Z. Feng, K. H. Lee and Q. Wang, *J. Mech. Phys. Solids*, 2020, **137**, 103831.
62 W. Kuhn, *Kolloid-Z.*, 1942, **101**, 248–271.
63 W. Zhao, MS thesis, University of Akron, 2018.
64 M. M. Nava, M. T. Raimondi and R. Pietrabissa, *Biomed Res. Int.*, 2012, **2012**, 797410.
65 J. Wang, J. A. Kaplan, Y. L. Colson and M. W. Grinstaff, *Adv. Drug Delivery Rev.*, 2017, **108**, 68–82.
66 S. Lin, J. Ni, D. Zheng and X. Zhao, *Extreme Mech. Lett.*, 2021, **48**, 101399.